Research in Astron. Astrophys. **2013** Vol. **13** No. **1**, 28 – 38
http://www.raa-journal.org *http://www.iop.org/journals/raa*

Research in Astronomy and Astrophysics

A multi-transition molecular line study of infrared dark cloud G331.71+00.59

Nai-Ping Yu and Jun-Jie Wang

National Astronomical Observatories, Chinese Academy of Sciences, Beijing 100012, China; *yunaiping09@mails.ucas.ac.cn*
NAOC-TU Joint Center for Astrophysics, Lhasa 850000, China

Received 2012 March 12; accepted 2012 August 3

Abstract Using archive data from the Millimeter Astronomy Legacy Team Survey at 90 GHz (MALT90), carried out using the Mopra 22-m telescope, we made the first multi-transition molecular line study of infrared dark cloud (IRDC) MSXDC G331.71+00.59. Two molecular cores were found embedded in this IRDC. Each of these cores is associated with a known extended green object (EGO), indicating places of massive star formation. The HCO^+ (1–0) and HNC (1–0) transitions show prominent blue or red asymmetric structures, suggesting outflow and inflow activities of young stellar objects (YSOs). Other detected molecular lines include $H^{13}CO^+$ (1–0), C_2H (1–0), HC_3N (10–9), HNCO($4_{0,4}$–$3_{0,3}$) and SiO (2–1), which are typical of hot cores and outflows. We regard the two EGOs as evolving from the IRDC to hot cores. Using public GLIMPS data, we investigate the spectral energy distribution of EGO G331.71+0.60. Our results support this EGO being a massive YSO driving the outflow. G331.71+0.58 may be at an earlier evolutionary stage.

Key words: stars: formation — ISM: outflows — ISM: molecules

1 INTRODUCTION

Infrared dark clouds (IRDCs) were first discovered in the mid 1990s by the two infrared satellites ISO (Perault et al. 1996) and MSX (Egan et al. 1998) as silhouettes against the bright mid-infrared Galactic background. Simon et al. (2006) identified 10 931 candidate IRDCs based on the MSX 8 μm data of the Galactic plane from $\ell = 0^\circ - 360^\circ$ and $|b| \leq 5^\circ$. IRDCs are predominantly found in the first and fourth Galactic quadrants and near the Galactic mid-plane (Jackson et al. 2008), where the mid-infrared background is greatest. Molecular line and dust continuum studies of IRDCs have shown that they are cold (<25 K), dense ($n(\mathrm{H_2}) > 10^5$ cm^{-3}, $N(\mathrm{H_2}) > 10^{22}$ cm^{-2}), and massive ($\sim 10^2 - 10^5 M_\odot$) structures with sizes of $\sim$ 1.15 pc. However, only small samples of the IRDCs originally published by Simon et al. (2006) have been investigated.

Cyganowski et al. (2008) identified more than 300 Galactic extended 4.5 μm sources, naming them extended green objects or "green fuzzies" due to the common color coding of the 4.5 μm band as green in three-color images of the Spitzer Infrared Array Camera (IRAC). Those researchers have suggested that the 4.5 μm IRAC band offers a promising new approach for identifying massive young stellar objects (MYSOs) with outflows, which are believed to be due to H_2 (ν = 0–0, S (9, 10, 11)) lines and CO ($\nu = 1-0$) band heads (Reach et al. 2006). The majority of extended green objects

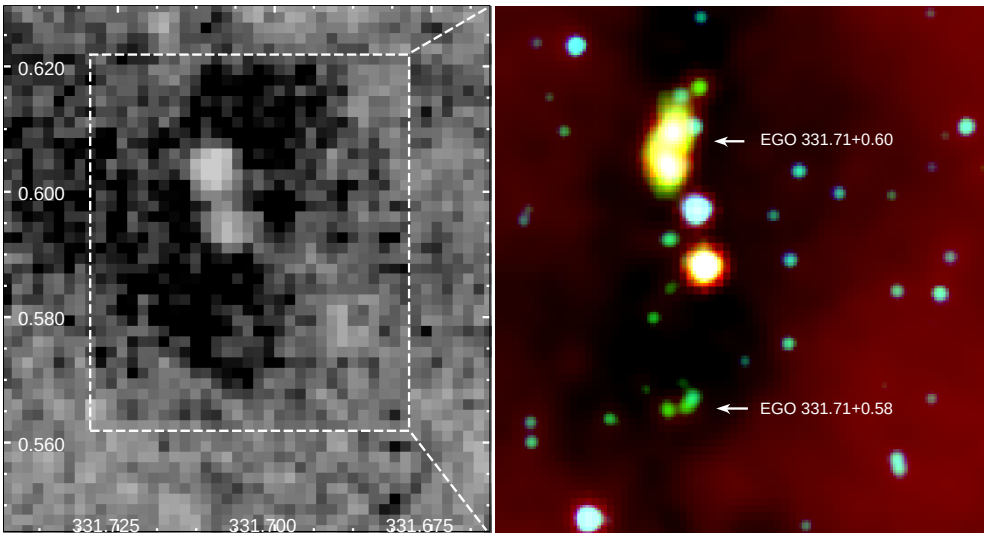

Fig. 1 *Left*: MSX A band image of IRDC G331.71+00.59. *Right*: Three color images of this IRDC: 8 μm emission in red, 4.5 μm emission in green and 3.6 μm emission in blue. The two EGOs within this IRDC are marked.

(EGOs) are associated with IRDCs. The infrared dark cloud MSXDC G331.71+00.59 (Fig. 1) has almost never been studied even after it was found to be associated with two EGOs: G331.71+0.58 and G331.71+0.60 (hereafter G0.58 and G0.60). We present the first molecular line study of this source. The distance of G331.71+00.59 is still unknown. According to the Galactic rotation model of Fich et al. (1989) (with $R_\odot = 8.2$ kpc and $v_\odot = 220$ km s^{-1}), we obtain a kinematic distance of either 4.26 kpc or 10.70 kpc. This ambiguity arises because we are studying a region in the fourth Galactic quadrant, where a given velocity may be associated with two possible distances. As IRDCs are silhouettes against the Galactic background, we use the near distance of 4.26 kpc in the following analysis.

2 DATA

The Millimeter Astronomy Legacy Team 90 GHz survey is a large international project aimed at characterizing sites within our Galaxy where high-mass stars will form. The survey covers a Galactic longitude range of $\sim -60°$ to $\sim 15°$ and Galactic latitude range of –1° to +1°. The observations were carried out with the newly upgraded Mopra Spectrometer (MOPS). The full 8 GHz bandwidth of MOPS was split into 16 zoom bands of 138 MHz each providing a velocity resolution of $\sim$ 0.11 km s^{-1}. The angular resolution of Mopra is about 38 arcsec, with beam efficiency between 0.49 at 86 GHz and 0.42 at 115 GHz (Ladd et al. 2005).

The central frequencies of transitions we selected to study in the paper are shown in Table 1. More information about this survey can be found through the MALT90 website (*http://malt90.bu.edu*). The data processing is conducted using Gildas and line parameters (peak intensity, central velocity and FWHM) are obtained by Gaussian fitting.

To complement the molecular data, we used data from the Galactic Legacy Infrared Mid-Plane Survey Extraordinaire (GLIMPSE) survey of Spitzer to study young stellar objects (YSOs) in the region.

Table 1 List of the Transitions Selected for Study in this Paper

Species	Transition	ν (GHz)	Primary Information Provided
HCO^+	(1–0)	89.189	High column density, kinematics
$H^{13}CO^+$	(1–0)	86.754	High column density, optical depth
HNC	(1–0)	90.663	High column density, cold gas
HC_3N	(10–9)	91.200	Hot core
HNCO	($4_{0,4}$–$3_{0,3}$)	87.925	Hot core
C_2H	(1–0)	87.317	Photodissociation region
SiO	(2–1)	86.847	Shock/outflow

3 RESULTS AND DISCUSSION

Figure 1 (left) shows the MSX A band image of MSXDC G331.71+00.59. The locations of two EGOs are displayed on the right composite image of Spitzer: 3.6 μm in blue, 4.5 μm in green and 8.0 μm in red. G0.60 shows a larger size than G0.58.

3.1 Molecular Lines

Figure 2 shows the molecular line spectra obtained towards G0.60 and G0.58. It is worth noting that a single-gaussian fit is insufficient for the optically thick molecular lines of HCO^+ and HNC in the two sources that show prominent blue or red asymmetric structures. A blue asymmetric structure, called a "blue profile," a combination of a double peak with a brighter blue peak or a skewed single blue peak in optically thick lines (Mardones et al. 1997), has been found in HCO^+ lines. This blue line asymmetry in an optically thick tracer such as HCO^+ is often suggestive of infall (i.e., Sun & Gao 2009). Surely a blue profile may also be caused by rotation and outflow. However, infall motion is the only process that would consistently produce the blue profile. Outflow and rotation only produce a blue asymmetric line profile along a particular line of sight (LOS) to a source (Sun & Gao 2009).

Figure 3 shows a mapping observation of HCO^+ in G0.58. The mapping observation allows us to confirm inflow activities in this region. G0.60 has a similar image and is omitted from display here. Detections of the optically thin line of $H^{13}CO^+$ help us to determine the central velocity referred to as the local standard of rest, $V_{\rm LSR}$. The parameters determined from Gaussian fitting of these lines are presented in Table 2. To quantify the blue profile, we further use an asymmetry parameter δV defined as the difference between the peak velocity of an optically thick line V(thick) and an optically thin line V(thin) in units of the optically thin line FWHM (full width at half maximum) dV(thin): $\delta V = \frac{V(\rm thick)-V(\rm thin)}{dV(\rm thin)}$. Mardones et al. (1997) adopted a criterion $\delta V < -0.25$ for indicating the blue profile. Our calculations demonstrate the blue profile is caused by inflow in this IRDC.

3.1.1 Column densities and masses

We derive the molecular column densities of HCO^+ and hence masses in the region assuming optically thick HCO^+ and optically thin $H^{13}CO^+$ lines, and local thermodynamic equilibrium (LTE). We calculate the excitation temperature from

$$T_{\rm ex} = \frac{h\nu_0}{k}\Big[\ln\Big(1+\frac{h\nu_0/k}{T_{\rm max}({\rm HCO^+})+J_v(T_{\rm bg})}\Big)\Big]^{-1}, \quad (1)$$

where ν_0 is the rest frequency, $T_{\rm bg}$ is temperature of the background radiation (2.73 K) and

$$J_v(T) = \frac{h\nu_0}{k}\frac{1}{(e^{h\nu_0/kT}-1)}. \quad (2)$$

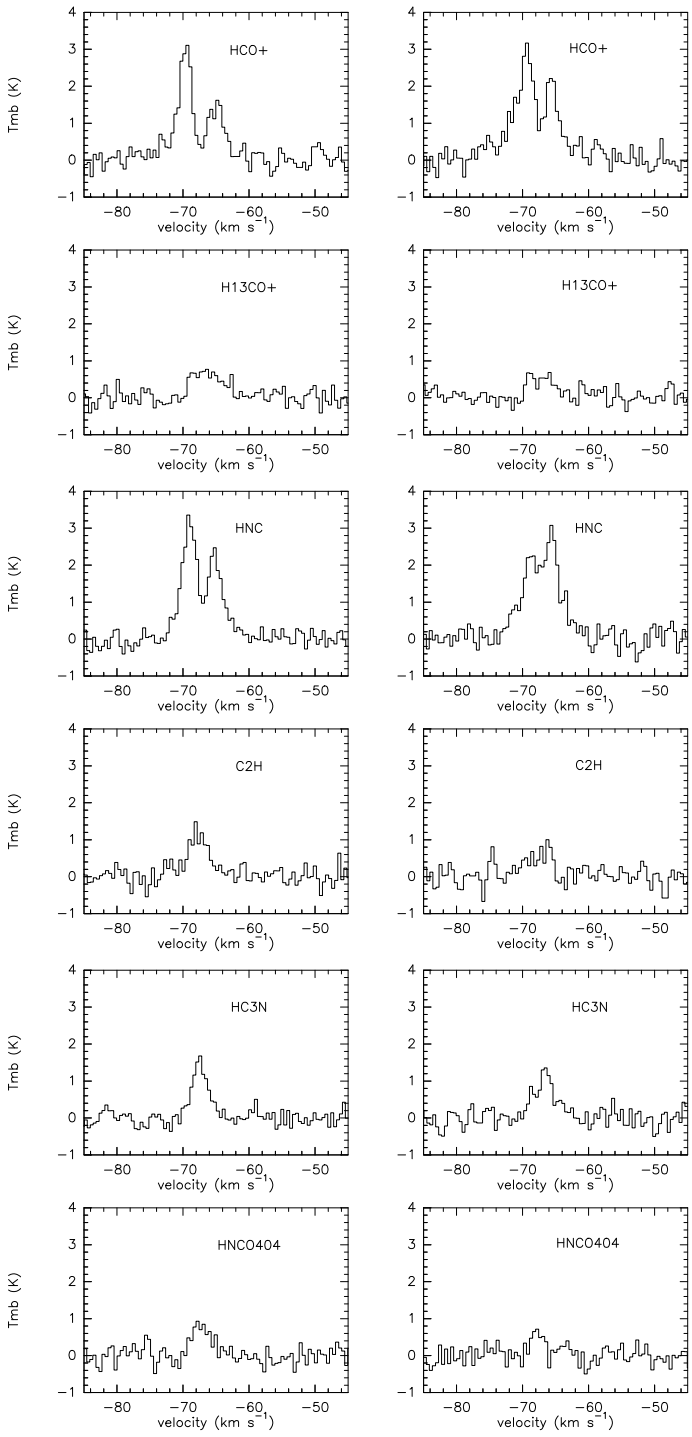

Fig. 2 Spectra towards the center of G0.60 (*left*) and G0.58 (*right*). The vertical axis is the main beam brightness temperature.

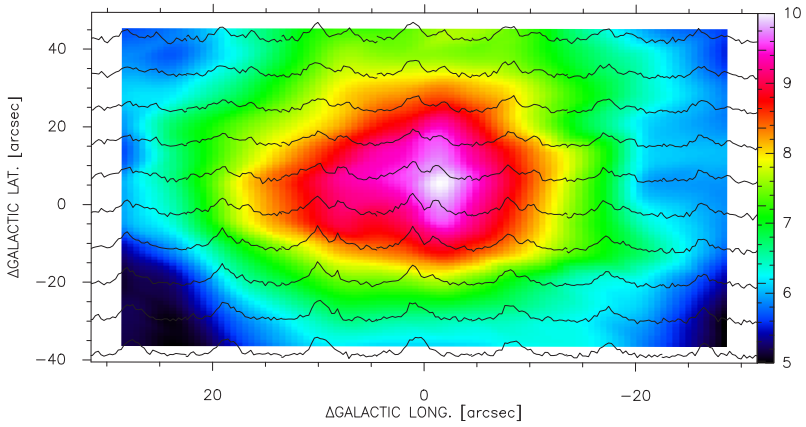

Fig. 3 HCO^+ spectra superimposed on its integrated map obtained towards G0.58.

Table 2 Observed Parameters of the Molecular Lines Shown in Fig. 2

Source	Emission	$T_{\rm mb}$ (K)	$V_{\rm LSR}$ (km s^{-1})	FWHM (km s^{-1})
G0.60	HCO^+	3.07 ± 0.08	-69.66 ± 0.06	2.38 ± 0.16
		1.52 ± 0.05	-64.96 ± 0.13	2.88 ± 0.31
	$H^{13}CO^+$	0.97 ± 0.12	-66.32 ± 0.30	5.30 ± 0.61
	HNC	3.18 ± 0.06	-69.06 ± 0.05	2.66 ± 0.13
		2.23 ± 0.09	-65.10 ± 0.07	2.70 ± 0.22
	C_2H	1.15 ± 0.12	-67.71 ± 0.17	3.77 ± 0.52
	HC_3N	1.51 ± 0.08	-67.43 ± 0.09	2.80 ± 0.22
	HNCO	0.86 ± 0.05	-67.23 ± 0.22	3.22 ± 0.47
G0.58	HCO^+	2.62 ± 0.40	-69.56 ± 0.10	3.87 ± 0.34
		2.06 ± 0.20	-65.41 ± 0.11	2.14 ± 0.26
	$H^{13}CO^+$	0.59 ± 0.03	-67.08 ± 0.37	4.36 ± 0.71
	HNC	1.93 ± 0.20	-68.81 ± 0.36	4.05 ± 0.77
		2.30 ± 0.25	-65.38 ± 0.21	3.00 ± 0.43
	C_2H	0.65 ± 0.10	-67.50 ± 0.42	4.49 ± 0.91
	HC_3N	1.12 ± 0.15	-66.67 ± 0.18	38.2 ± 0.46
	HNCO	0.71 ± 0.08	-67.80 ± 0.20	2.04 ± 0.41

We also assume that the HCO^+ and $H^{13}CO^+$ emission arises from the same gas and shares a common excitation temperature. The optical depth of the $H^{13}CO^+$ line may be found from

$$\tau = -\ln\left[1 - \frac{T_{\rm max}(H^{13}CO^+)}{[J_v(T_{\rm ex}) - J_v(T_{\rm bg})]}\right] . \quad (3)$$

Then we use equations (2) and (5) in Purcell et al. (2006) to find the total $H^{13}CO^+$ column densities. Using $M = \mu\, m_{\rm H}\, d^2\, \Omega\, {\rm X}(H^{13}CO^+)^{-1}\, N(H^{13}CO^+)$, we obtain the masses for the two cores, where $N(H^{13}CO^+)$ is the $H^{13}CO^+$ column density, d is the distance, and $m_{\rm H}$ is the mass of a hydrogen atom. We adopt a mean molecular weight per H_2 molecule of $\mu = 2.72$ to include helium, and Ω is the area of the two cores. For $H^{13}CO^+$, we adopt an abundance of 2×10^{-10} relative to H_2 (Vogel et al. 1984; Rawlings et al. 2004; Purcell et al. 2006; Klaassen & Wilson 2007). Using the above methods we obtain results for $T_{\rm ex}$ of 5.9 K and 5.6 K. These values are considerably lower than the temperatures of $\sim$15 K quoted in previous work and we conclude that the emission was beamed in a significant fraction of the observations. In the following analysis we have assumed an excitation temperature of 15 K for HCO^+.

Table 3 Derived Parameters of G0.60 and G0.58

Source	$T_{\rm ex}$ (HCO^+) (K)	τ ($H^{13}CO^+$)	N ($H^{13}CO^+$) (10^{13} cm^{-2})	M ($10^3 M_\odot$)
G0.60	5.9	0.08	3.6	1.9
G0.58	5.6	0.05	2.3	0.9

The final results are listed in Table 3. The high column densities suggest that massive stars are forming. Recent theoretical work predicts a mass column density threshold >1 g cm^{-2} for massive star formation (Krumholz & McKee 2008; Krumholz et al. 2010).

3.1.2 Outflow

It should be noted that the central HNC spectra of G0.58 show a red profile. The origin of the red profile could be caused by outflows or rotations of molecular gas. As EGOs are probably MYSOs driving outflows, outflow activities could exist in this region.

Figure 4 presents the HNC (solid line) and $H^{13}CO^+$ (dashed line) spectra towards the center of G0.58 and G0.60. The line wings of HNC are obvious. The existence of outflow is further confirmed by the position-velocity (PV) diagrams shown in Figure 4.

Figure 5 shows the map of the molecular outflow traced by the HNC line; plotted are the intensities integrated over the velocity ranges that are lower and higher than the systematic velocity, i.e., red and blue shifted emission respectively. The red and blue contours represent blue and red lobes of the outflow. From the HNC map it can be noted that the lobes are nearly unresolved by our observations, and that high resolution is needed to determine parameters such as the collimation factor and inclination angles of the outflows. Assuming that HNC emission in the line wings is optically

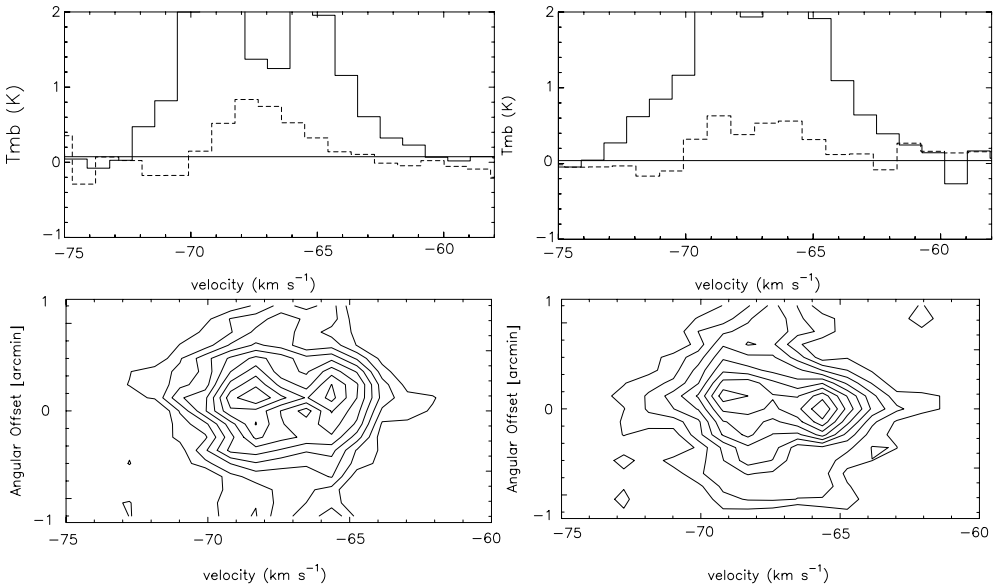

Fig. 4 *Top*: Enlarged view of the HNC (*solid line*) and $H^{13}CO^+$ (*dashed line*) profiles presented in Fig. 2 in the intensity range going from -1 to 2 K. *Bottom*: position-velocity diagram cut along the east-west direction (shown in Fig. 5) constructed from the HNC transition of G0.60 and G0.58. Contour levels are 20%, 30%, ..., 90% of the center.

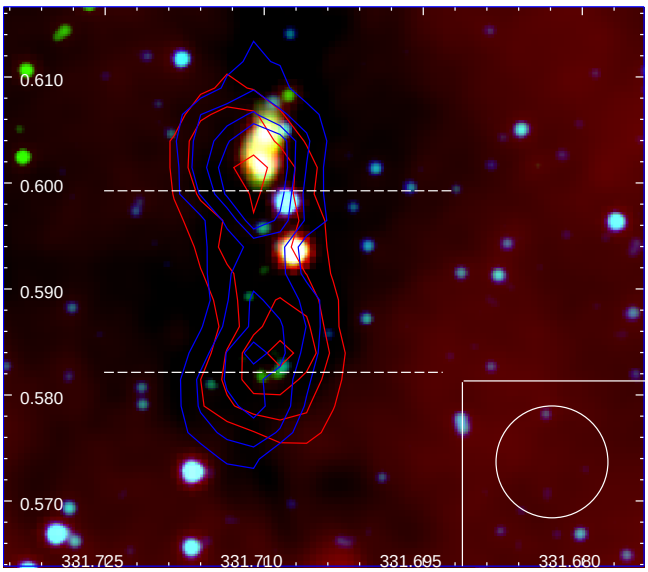

Fig. 5 Spitzer image of the region around IRDC G331.75+00.59. The blue and red contours represent the integrated intensity of the HNC transition in the blue and red shifted wings respectively. Contour levels are 3.6, 4.6, 5.6, and 6.6 K km s^{-1}. The two white dashed lines are the position and orientation where the PV diagrams shown in Fig. 4 were computed.

thin, with X(HNV) = [HNC]/[H_2] = 10^{-8} (Turner et al. 1997) and $T_{\rm ex}$ = $h\nu_0/k$ =4.36 K, we derive its column density from

$$N({\rm HNC}) = Q(T_{\rm ex})\frac{8\pi\nu_0^3}{c^3}\frac{g_l}{g_u}\frac{1}{A_{ul}}[1-e^{-h\nu_0/kT_{\rm ex}}]^{-1}\int \tau dv, \quad (4)$$

where ν_0, $g_{\rm u}$, $g_{\rm l}$ and $A_{\rm ul}$ are the rest frequency, the upper and lower level degeneracies and the Einstein's coefficient of HNC respectively. $Q(T_{\rm ex})$ is the partition function and c is the speed of light. On the other hand, by assuming that HNC emission is optically thin in the line wings, we use the approximation

$$\int \tau dv = \frac{1}{J(T_{\rm ex})-J(T_{\rm bg})}\int T_{\rm mb} dv. \quad (5)$$

The derived parameters are shown in Table 4.

Table 4 Outflow Parameters

Source	Shift	Δv (km s^{-1})	N (HNC) (10^{13} cm^{-2})	M ($M_\odot$)
G0.60	red	(−66, −60)	1.5	15.8
	blue	(−75, −69)	1.3	13.7
G0.58	red	(−66, −60)	1.9	20.0
	blue	(−75, −69)	1.1	11.6

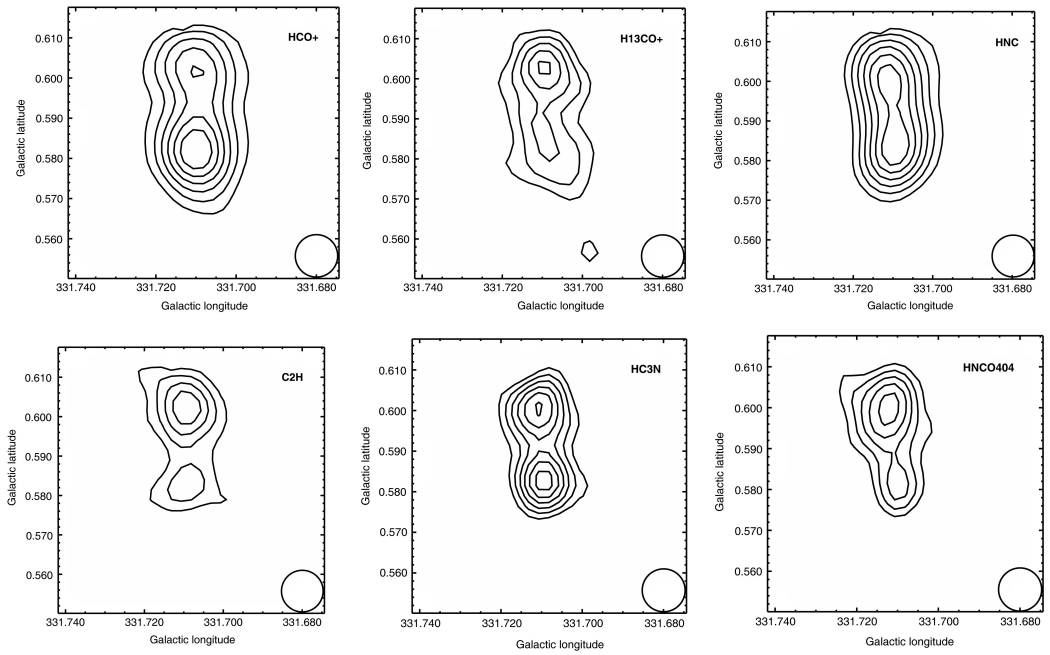

Fig. 6 Maps of the integrated intensity of the six transitions. The contour levels are all 30%, 40%, ..., 90% of each peak. The beam of the Mopra telescope at the observation frequency is shown in the right corner.

3.1.3 Other lines and SiO

The ethynyl radical (C_2H) was first detected in interstellar clouds by Tucker et al. (1974). Observations indicate that C_2H is produced in photodissociation regions (PDRs) (e.g., Lo et al. 2009; Gerin et al. 2011) and is almost omnipresent toward evolutionary stages from IRDCs via high-mass protostellar objects (HMPOs) to ultracompact HII regions (UCHII) (Huggins et al. 1984; Beuther et al. 2008). The stronger emission of C_2H in G0.60 than in G0.58 (Fig. 6) suggests G0.58 to be in an earlier evolutionary stage. This was further confirmed by the carbon-bearing species HNCO, which is typically only seen in the hot cores around high-mass protostars once molecules have been liberated off dust grains by radiation or shocks (Brown et al. 1988). HC_3N is an excellent tracer of dense gas (Chung et al. 1991; Bergin et al. 1996) as it has high electric dipole moments ($\mu = 3.72$ Debye). It is also a tracer of a hot core because it can be easily destroyed by ultraviolet (UV) photons from central ionizing stars (Brown et al. 1988). Thus we regard the two EGOs to be evolving from IRDCs to hot cores.

SiO is known to be greatly enhanced in outflows and shocked regions (Martin-Pintado et al. 1992) since, in the general interstellar medium, Si is frozen out onto dust grains. When the gas in a region is shocked, for example the gas through which a protostellar outflow is passing or due to the expansion of the PDR, the dust grains can sublimate and Si is released into the gas phase. Models and observations of SiO in PDRs around regions with formation of massive stars suggest moderate SiO enhancement. Schilke et al. (2001) found SiO column densities of $\sim 10^{12}$ cm^{-2} in their observed PDRs. Again, by assuming SiO is optically thin and in LTE, we calculated the column density by using the method described in Section 3.1.2. The high SiO column densities (12.2×10^{14} cm^{-2} for G0.60 and 18.6×10^{14} cm^{-2} for G0.58) suggest that the SiO emission we observed does come

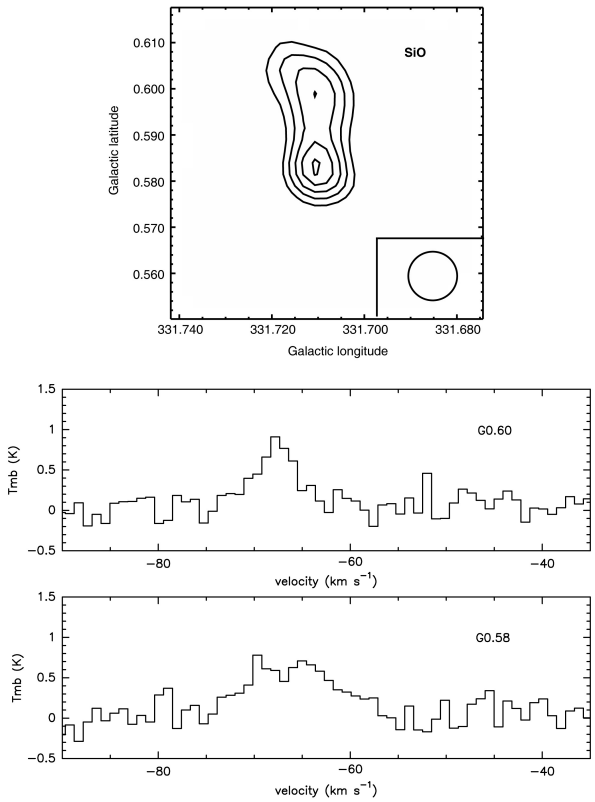

Fig. 7 *Top*: Integrated intensity map of SiO. Contour levels are 30%, 40%, ..., 90% of the peak. *Bottom*: SiO spectra towards the center of G0.60 and G0.59.

primarily from outflow shocks. The large line width of SiO ($>$ 10 km s^{-1}) further supports our suggestions. Figure 7 shows the integrated intensity map of SiO and spectra towards the center of G0.60 and G0.58.

3.2 Spectral Energy Distribution

According to Cyganowski et al. (2008), the mid-IR colors of EGOs lie in regions of a color-color diagram (CCD) occupied by young protostars still embedded in infalling envelopes. In this section, we try to fit the spectral energy distribution (SED) of these two EGOs using the tool developed by Robitaille et al. (2007). Briefly, the SED-fitting tool works as a regression method to find the SEDs within a specified χ^2 from a large grid of models after fitting the input data points. The grid of models contains stellar masses, disk masses, mass accretion rates and LOS inclinations. The grid of YSO models was computed by Robitaille et al. (2006) using the 20 000 two-dimensional radiation transfer models from Whitney et al. (2003a,b, 2004). Each YSO model has SEDs for 10 viewing angles (inclinations), so the total YSO grid consists of 200 000 SEDs. We use the fluxes in the four Spitzer IRAC bands and MIPS in 24 μm from Cyganowski et al. (2008). The 4.5 μm band is used as an upper limit, considering that it is blended with emissions from outflows. The upper-left panel in Figure 8 shows the SEDs of the 20 best fitting models of G0.60. The solid black line represents

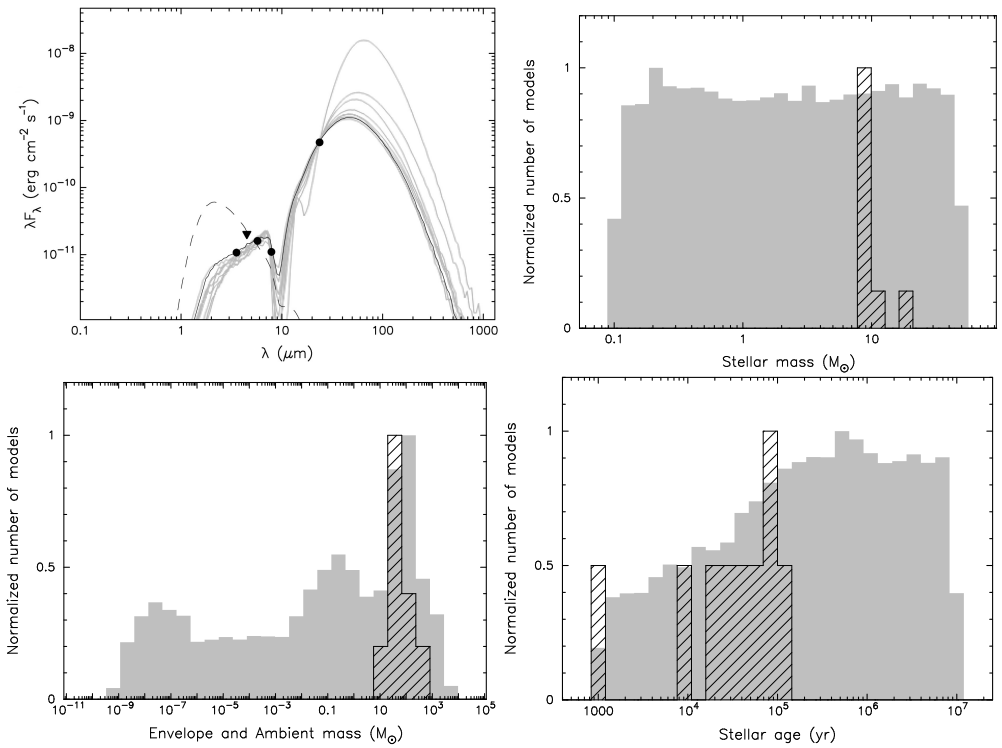

Fig. 8 Spectral energy distributions of G0.60 and distributions of some physical parameters (central source mass, envelope mass and age) of the best fitting models (*hashed columns*) together with the distribution of all the models (*grey columns*).

the best fitting model from which we obtain a central mass of $\sim 10\ M_{\odot}$. The SED fitting result of G0.58 is not good enough, due to large errors in 5.8 μm and 8.0 μm (Cyganowski et al. 2008).

Figure 8 also presents the histograms with the distribution of the constrained physical parameters. The hashed columns represent the 20 best fitting models and the gray columns correspond to all the models of the grid. Although there is a high dispersion in the age, the presence of a massive envelope is strong evidence that the source is at an early evolutionary stage. We note that an MYSO(s) is forming in G0.60.

4 SUMMARY

Using archive data from the MALT90, we made a first multi-transition molecular line study of IRDC MSXDC G331.71+00.59, where two EGOs are embedded. Two molecular cores were found to be associated with these EGOs. The HCO^+ (1–0) and HNC (1–0) transitions show outflow and/or inflow activities of YSOs. By analysis of other molecules, including $H^{13}CO^+$ (1–0), C_2H (1–0), HC_3N (10–9) and HNCO ($4_{0,4} - 3_{0,3}$), we regard the two EGOs to be evolving from the IRDC to hot cores. Using public GLIMPS data, we investigate the spectral energy distribution of EGO G331.71+0.60, with the results supporting the EGO being an MYSO driving outflows. EGO G331.71+0.58 may be in an earlier evolutionary stage. Moreover, given its location in the sky, G331.71+0.58 will be easily accessible in the near future for high linear resolution studies with ALMA.

Acknowledgements We thank the MALT90 project team for the observations. We are also grateful to the anonymous referee for his/her constructive suggestions.

References

Bergin, E. A., Snell, R. L., & Goldsmith, P. F. 1996, ApJ, 460, 343
Beuther, H., Semenov, D., Henning, T., & Linz, H. 2008, ApJ, 675, L33
Brown, P. D., Charnley, S. B., & Millar, T. J. 1988, MNRAS, 231, 409
Chung, H. S., Osamu, K., & Masaki, M. 1991, Journal of Korean Astronomical Society, 24, 217
Cyganowski, C. J., Whitney, B. A., Holden, E., et al. 2008, AJ, 136, 2391
Egan, M. P., Shipman, R. F., Price, S. D., et al. 1998, ApJ, 494, L199
Fich, M., Blitz, L., & Stark, A. A. 1989, ApJ, 342, 272
Gerin, M., Kaźmierczak, M., Jastrzebska, M., et al. 2011, A&A, 525, A116
Huggins, P. J., Carlson, W. J., & Kinney, A. L. 1984, A&A, 133, 347
Jackson, J. M., Finn, S. C., Rathborne, J. M., Chambers, E. T., & Simon, R. 2008, ApJ, 680, 349
Klaassen, P. D., & Wilson, C. D. 2007, ApJ, 663, 1092
Krumholz, M. R., Cunningham, A. J., Klein, R. I., & McKee, C. F. 2010, ApJ, 713, 1120
Krumholz, M. R., & McKee, C. F. 2008, Nature, 451, 1082
Ladd, N., Purcell, C., Wong, T., & Robertson, S. 2005, PASA, 22, 62
Lo, N., Cunningham, M. R., Jones, P. A., et al. 2009, MNRAS, 395, 1021
Mardones, D., Myers, P. C., Tafalla, M., et al. 1997, ApJ, 489, 719
Martin-Pintado, J., Bachiller, R., & Fuente, A. 1992, A&A, 254, 315
Perault, M., Omont, A., Simon, G., et al. 1996, A&A, 315, L165
Purcell, C. R., Balasubramanyam, R., Burton, M. G., et al. 2006, MNRAS, 367, 553
Rawlings, J. M. C., Redman, M. P., Keto, E., & Williams, D. A. 2004, MNRAS, 351, 1054
Reach, W. T., Rho, J., Tappe, A., et al. 2006, AJ, 131, 1479
Robitaille, T. P., Whitney, B. A., Indebetouw, R., Wood, K., & Denzmore, P. 2006, ApJS, 167, 256
Robitaille, T. P., Whitney, B. A., Indebetouw, R., & Wood, K. 2007, ApJS, 169, 328
Schilke, P., Pineau des Forêts, G., Walmsley, C. M., & Martín-Pintado, J. 2001, A&A, 372, 291
Simon, R., Jackson, J. M., Rathborne, J. M., & Chambers, E. T. 2006, ApJ, 639, 227
Sun, Y., & Gao, Y. 2009, MNRAS, 392, 170
Tucker, K. D., Kutner, M. L., & Thaddeus, P. 1974, ApJ, 193, L115
Turner, B. E., Pirogov, L., & Minh, Y. C. 1997, ApJ, 483, 235
Vogel, S. N., Wright, M. C. H., Plambeck, R. L., & Welch, W. J. 1984, ApJ, 283, 655
Whitney, B. A., Wood, K., Bjorkman, J. E., & Cohen, M. 2003a, ApJ, 598, 1079
Whitney, B. A., Wood, K., Bjorkman, J. E., & Wolff, M. J. 2003b, ApJ, 591, 1049
Whitney, B. A., Indebetouw, R., Bjorkman, J. E., & Wood, K. 2004, ApJ, 617, 1177